JOURNAL OF THERMOPHYSICS AND HEAT TRANSFER
Vol. 16, No. 2, April–June 2002

Rarefaction, Compressibility, and Viscous Heating in Gas Microfilters

Imtiaz Ahmed* and Ali Beskok†
Texas A&M University, College Station, Texas 77843-3123

Gas flows through microfilters are simulated in the continuum and slip flow regimes as a function of the Knudsen, Reynolds, and Mach numbers. The numerical simulations are based on the spectral element formulation of compressible Navier–Stokes equations, which utilize previously developed high-order velocity slip and temperature jump boundary conditions. Both slip and no-slip simulations are used to identify the rarefaction effects. The simulation results show skin friction and form-drag reduction with increased Knudsen number. Pressure drops across the filters are compared against several empirical scaling laws, available in the literature. Compressibility becomes important for high-speed flows, creating large density fluctuations across the microfilter elements. For high-Mach-number flows interactions between thermal and kinetic energies of the fluid are observed. It is also shown that viscous heating plays a significant role for high-speed gas flows, which impact heat-transfer characteristics of microfilters.

Nomenclature

h = filter hole diameter
i = free index, $i = 1, 2, 3$
j = free index, $j = 1, 2, 3$
K = normalized pressure drop
Kn = Knudsen number based on the outlet mean free path and the filter diameter h
L = center-to-center filter separation distance
$\boldsymbol{n}$ = surface normal
Pr = Prandtl number
p = pressure
q = heat flux
R = specific gas constant
Re = Reynolds number based on mass flow rate per filter width
T = temperature
t = filter thickness
u = velocity
w = filter width
β = filter opening factor
γ = ratio of specific heats
λ = mean free path
μ = dynamic viscosity
ρ = density
σ_T = energy accommodation coefficient
σ_v = tangential momentum accommodation coefficient
τ_s = shear stress

Subscripts

in = inlet conditions
n = normal direction to the surface
out = outlet conditions
s = slip conditions
w = wall conditions
λ = conditions, one mean free path away from the surface

Superscripts

$*$ = normalized quantity
$-$ = channel averaged quantity

Introduction

GAS microfilter systems can be used for detection of airborne biological and chemical entities and for environmental monitoring applications. Recent advancements in microfabrication technologies enabled development of sufficiently thin filters that are strong enough to provide useful flow rates under large pressure drops.[1] Motivated by these developments, several research groups started to investigate gas flows through microfilter systems.[2–4] Analysis of gas flows through microfilters requires consideration of three fundamental issues: rarefaction, compressibility, and geometric complexity.

The rarefaction is caused by the small characteristic length scales of microfilters h that are comparable to the local mean free path λ. This leads to definition of the Knudsen number $Kn = \lambda/h$, where increased values of Kn show deviations from the continuum hypothesis. Depending on the Knudsen number, we observe four different flow regimes: continuum ($Kn < 0.01$); slip ($0.01 < Kn < 0.1$); transitional ($0.1 < Kn < 10$); and free molecular ($Kn > 10$). The local mean free path of the gas can be calculated using

$$\lambda = (\mu/\rho)\sqrt{\pi/2RT}$$

The mean free path of air under standard conditions is $\lambda = 65$ nm. Therefore, microfilters with characteristic hole diameter larger than 0.65 μm operate in the slip and continuum flow regimes, which is the focus of the current study.

The compressibility effects are important when there are large (more than 10%) density variations in the microfluidic system. This particularly happens when there are significant pressure and/or temperature fluctuations or at high-speed flows. These conditions are observed in micronozzles, and they might also become important for the microfilters. Even for low-speed constant-area microchannel flows gas compressibility cannot be neglected. Significant pressure drop from inlet to the exit affects the density variation in the channel.[5–10]

The geometric complexity of microfilters is also important. In the simplest form the microfilters are very short channels or sudden constrictions in the flowfield. Therefore, simple analysis based on the fully developed flow assumption cannot be used. Furthermore, the

---

Received 6 July 2001; revision received 24 October 2001; accepted for publication 24 October 2001.

[*] Graduate Student, Mechanical Engineering Department; currently Test Engineer, Fluent, Inc., Evanston, IL 60201.

[†] Assistant Professor, Mechanical Engineering Department, 3123 Tamu; abeskok@mengr.tamu.edu. Member AIAA.

filter holes have complicated shapes, such as rectangular, hexagonal, circular, elliptic, or square. Filters can also have geometric variations along the filter thickness, sharp or smooth inlets and exits. The side-wall geometry is shown to affect the overall pressure drop across the microfilter devices.[3]

Empirical formulas for pressure drop in conventional filters have been obtained previously.[11,12] However these scaling laws are valid for high-Reynolds-number flows ($Re \gg 100$), and they can not be applied to microfilters.[3] The initial work on microfilters is by Kittilsland et al.,[13] who fabricated a filter that consisted of two silicon membranes with holes. By changing the membrane separation distance, they were able to build filters for separation of particles as small as 50 nm. More recently, Yang et al.[2] developed a microelectromechanical-systems-based microfilter using a micron-thick silicon-nitride membrane coated with Parylene, which was used both to control the opening area of the filter and to provide strength. Experimental and numerical studies have shown that the flow in the microfilters strongly depends on the opening factor β (the ratio of the hole-area to the total filter area). Power requirements and the pressure drop through the microfilters have also been studied in Ref. 2. It has been shown that the power dissipation is a function of the opening factor, the ratio of the filter thickness to hole diameter, and the Reynolds number. The authors were able to fit their experimental and numerical simulation data to an empirically determined scaling law, given in the following[2]:

$$K = \beta^{-2}(t/h)^{0.28}[73.5/Re + 1.7] \tag{1}$$

where K is nondimensionalized pressure drop ($K = \Delta P/\frac{1}{2}\rho U_{\text{in}}^2$). The Reynolds number defined as

$$Re = \frac{\rho_{\text{in}} U_{\text{in}} h}{\mu \beta}$$

For a two-dimensional geometry the opening factor becomes the ratio of the hole opening length (diameter) to the center-to-center filter separation distance ($\beta = h/L$), resulting in

$$Re = \rho_{\text{in}} U_{\text{in}} L/\mu$$

Using the scaling law presented by Eq. (1) led to higher-pressure drops than the experimentally determined values. The assumptions and the parameters utilized in development of this scaling law were 1) two-dimensional geometry; 2) opening factor: $0.1 < \beta < 0.45$; 3) the t/h ratio: $0.08 < t/h < 0.5$; 4) Reynolds number: $1 < Re < 100$; and 5) Knudsen number: $0.006 < Kn < 0.013$, where $Kn = \lambda/h$.

More recently, Yang et al.[3] proposed the following modified scaling law based on detailed studies of the filter geometry, experimental data, and three-dimensional numerical simulations:

$$K = \beta^{-2}[3.5(t/h) + 3]\,[10.0/Re + 0.22] \tag{2}$$

Although most of the experimental data fit this relation, there were some deviations for low-Reynolds-number flows. This scaling law did not explicitly incorporate the rarefaction effects as a function of the Knudsen number. However, the rarefaction effects were included to the values of the constants because of the limited variations in Knudsen number.

Mott et al.[4] utilized two-dimensional direct-simulation Monte Carlo (DSMC) method to study gas transport through microfilters in the slip and early transition flow regimes and have shown that Yang's model became inaccurate in the transition flow regime, as well as for high-Reynolds-number flows. Based on the experimental data of Ref. 3 and their DSMC results, Mott et al.[4] proposed the following modified scaling law, which included the Knudsen number as an additional parameter:

$$K = \beta^{-2}\left(3.5\frac{t}{h} + 3\right)\left[\frac{10.}{Re} + 0.22\right]\left[\frac{0.0577}{0.0577 + Kn}\right] \tag{3}$$

The assumptions and parameters in their model were 1) two-dimensional geometry; 2) opening factor: $\beta = 0.25$; 3) the t/h ratio: 3; 4) Reynolds number: $0.2 < Re < 1$; and 5) Knudsen number: $0.0309 < Kn < 0.233$, where Kn is based on the inlet mean free path and the filter diameter. The t/h ratio used in Mott's studies were substantially larger than the values presented by Yang et al.[2,3]

The scaling laws presented in Eqs. (1–3) are developed starting from the fully developed Poiseuille flow assumption with added pressure drop corrections caused by the inlet and exit effects. Mott et al.[4] describes evolution of these scaling laws, including the slip flow corrections given as a function of the Knudsen number in Eq. (3). The coefficients used in Eqs. (1–3) are modified from the predictions given by simplified analytical models in order to match the experimental and numerical data.[2–4]

Here we must emphasize that previous studies did not address the compressibility and viscous dissipation effects in detail. The aforementioned empirical laws are based on the incompressible flow assumption, which might be inadequate to describe high-speed flows. Also, microfilter geometry is a sudden constriction in the flow path. Therefore, pressure drop caused by the fully developed (Poiseuille) flow might be negligibly small in thin microfilters. The purpose of our research is to systematically investigate the gas flow characteristics through microfilters as functions of the Reynolds, Mach, and Knudsen numbers.

Governing Equations and Boundary Conditions

Gas flows in the slip flow regime ($Kn < 0.1$) are governed by the compressible Navier–Stokes equations subject to the velocity slip[14] and temperature jump[15] boundary conditions, given in the following form:

$$u_s - u_w = \frac{2 - \sigma_v}{\sigma_v}\frac{\tau_s}{\rho(2RT_w/\pi)^{\frac{1}{2}}} \tag{4}$$

$$T_s - T_w = \frac{2 - \sigma_T}{\sigma_T}\left[\frac{2(\gamma - 1)}{(\gamma + 1)}\right]\frac{(-q_n)}{R\rho(2RT_w/\pi)^{\frac{1}{2}}} \tag{5}$$

where τ_s is the viscous stress component corresponding to the skin friction. The σ_v and σ_T are the tangential momentum and energy accommodation coefficients that determine effectiveness of tangential momentum and energy exchange of the molecules with the walls. Accommodation coefficients depend on the gas/surface pair and may vary with the surface roughness and temperature. In our studies we assumed full diffuse reflection both for the tangential momentum and energy exchange ($\sigma_v = \sigma_T = 1$). The slip and jump boundary conditions given by Eqs. (4) and (5) are first-order in Knudsen number. Beskok and Karniadakis derived an alternative high-order slip model in the following form[16,17]:

$$u_s = \tfrac{1}{2}[u_\lambda + (1 - \sigma_v)u_\lambda + \sigma_v u_w] \tag{6}$$

where u_λ is the streamwise component of the gas velocity, one mean free path away from the wall surface. A Taylor-series expansion of u_λ in the preceding equation captures Maxwell's first-order slip condition, along with higher-order corrections in Knudsen number. The corresponding high-order temperature jump boundary condition is

$$T_s = \frac{[(2 - \sigma_T)/Pr][2\gamma/(\gamma + 1)]T_\lambda + \sigma_T T_w}{\sigma_T + [(2 - \sigma_T)/Pr][2\gamma/(\gamma + 1)]} \tag{7}$$

where T_λ is the gas temperature one mean free path away from the surface and T_s is the gas (jump) temperature on the surface.

A schematic view of a rectangular microfilter array is shown in Fig. 1. In the current study we assumed that the filter width w is significantly larger than the filter height h so that the flowfield can be approximated to be two-dimensional. Considering that the filter holes repeat in a periodic fashion, we simulated gas flow through only one hole by imposing periodicity boundary conditions in the streamwise direction (Fig. 1). Here we must mention that for nonrectangular filters (elliptic, circular, or square) or for rectangular holes with small w/h ratio full three-dimensional simulations become necessary. Computational cost of the three-dimensional simulations compelled us to consider two-dimensional (simplified) geometry in the current study. In our simulations we fixed the height

Table 1 Dimensions of the microfilters used in this study

	Dimensions (μm)		
L_{ref}, μm	L	h	t
6	6	3.6	2.4
4	4	2.4	1.6
2	2	1.2	0.8
1	1	0.6	0.4

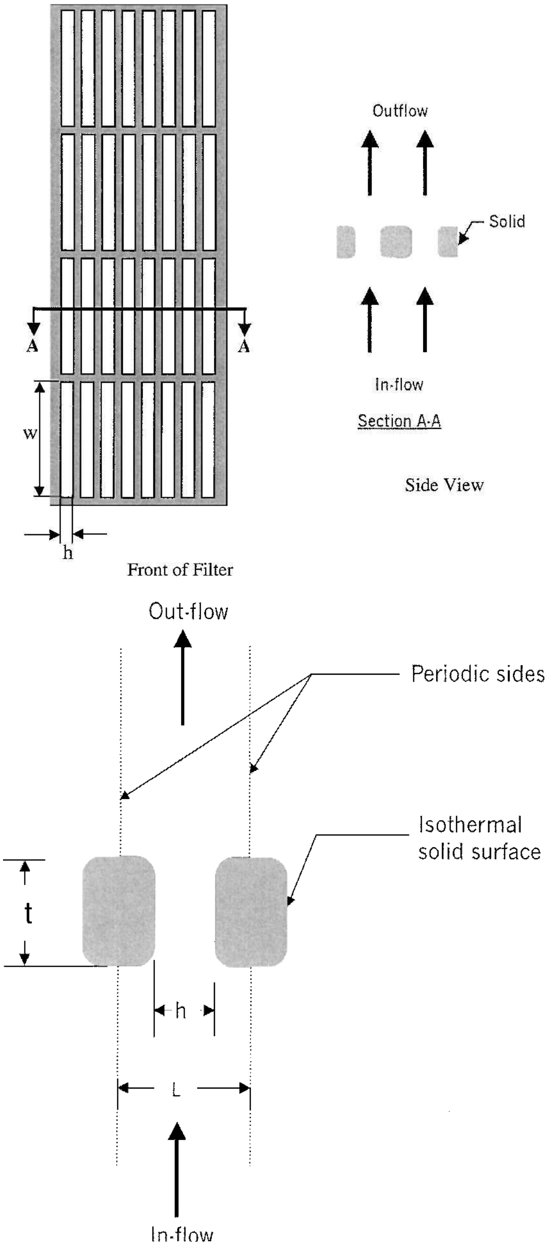

Fig. 1 Top: Schematic view of the microfilter (filter-front and cross-sectional views). Bottom: Schematic view of a simpified two-dimensional model. Various length scales are identified on the figure.

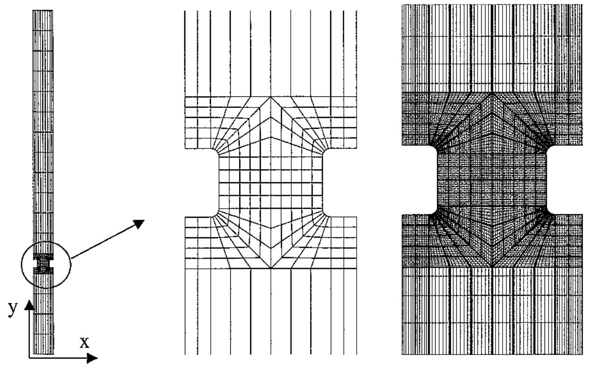

Fig. 2 Left: Elemental discretization of the entire flow domain consists of 360 spectral elements. Middle: Zoomed in view of the elemental discretization near the filter. Right: Spectral element mesh obtained using eighth-order Gauss–Lobatto–Legendre collocation points per direction, which results in 81 nodes per element.

h to the thickness t ratio of the hole opening ($h/t = 1.5$), as well as the opening factor $\beta = 0.6$ (height h to the center-to-center hole-separation distance L ratio). These dimensions are labeled in the bottom portion of Fig. 1. Using this fixed aspect ratio geometry, we varied the reference length scale L, creating a series of geometrically similar filters whose dimensions are tabulated in Table 1.

In our studies we utilized a two-dimensional spectral element algorithm μ-Flow, which solves the unsteady compressible Navier–Stokes equations subject to the high-order velocity slip and temperature-jump boundary conditions, given by Eqs. (6) and (7). The μ-Flow is based on the time splitting of the Navier–Stokes equations. The convective terms are discretized using a collocation algorithm, whereas the viscous terms are handled via a Galerkin projection. The μ-Flow utilizes Nth-order Gauss–Lobatto–Legendre polynomial expansions (per direction) in each element. Further details and validation of the algorithm, as well as formal derivation of high-order slip and temperature-jump boundary conditions, can be found in Ref. 17, pp. 224–239 and 53–62, respectively.

The flow domain was discretized using 360 nonuniform quadrilateral spectral elements, as shown in Fig. 2 (left). To test the convergence of our results, we successively utilized fourth-, sixth-, and eighth-order Gauss–Lobatto–Legendre polynomial expansions (per direction). This is known as the p-type mesh refinement, and it results in exponentially fast reduction of discretization errors (spectral convergence) for sufficiently smooth problems. Through the p-type grid refinement we did not observe significant differences between the sixth- and eighth-order results. Here we mostly present the eighth-order simulation results. Because μ-Flow is an unsteady flow solver, we had to ensure that our solution has reached a steady state. We monitored this by observing time history of the solution at various points in the domain, including the inflow and outflow regions. We also performed studies on the effects of the inflow/outflow boundaries in our solution and have taken these boundaries sufficiently away from the flow domain. Finally, in all of the simulations we monitored errors in the integral form of the conservation laws. The absolute maximum errors in the mass, momentum, and energy conservation equations are less than 0.07, 0.1, and 0.4%, respectively. The details of these grid independence, convergence, and inflow/outflow location studies can be found in Ref. 18.

Results and Discussion

The microfilter geometry is presented in Fig. 1. The surfaces shown in gray correspond to physical surfaces of the microfilter, where fully accommodating diffuse reflection boundary conditions are applied. The surfaces are kept at 300 K temperature. Using this basic geometry, we performed 32 different simulations by changing the inlet and exit conditions, as well as the reference length scale. To assess the rarefaction effects, we performed each simulation using both the no-slip and high-order slip conditions. The results are analyzed in terms of nondimensional parameters such as the Reynolds, Mach, and Knudsen numbers.

Rarefaction Effects

Rarefaction effects are investigated as a function of the Knudsen number by systematically decreasing the filter hole diameter h. Velocity slip and temperature jump are calculated in the domain using local thermodynamic variables, mean free path, and velocity gradients in dimensional form. To present the rarefaction effects, we organized our results using a reference Knudsen number based on the mean free path at the domain outlet and the filter hole diameter ($Kn = \lambda_{\mathrm{out}}/h$). The simulation conditions for the $h = 0.6$ μm case results in $Kn \approx 0.185$, which is above the accepted limit of slip flow theory ($Kn < 0.1$). Therefore, validity of our results for the smallest filter diameter case is questionable as a result of the breakdown of the Navier–Stokes equations in the early transitional flow regime. Despite this fact, it is our experience that transition between the slip and transitional flow regimes happens smoothly, as described by the Chapman–Enskog expansion procedure. Hence for $Kn < 0.2$ the simulation results cannot be too far from the slip flow predictions. Beskok and Karniadakis have shown through asymptotic analysis of the Burnett equations and DSMC simulations that for fully developed low-speed isothermal flows the Navier–Stokes equations with high-order slip conditions are sufficient to obtain accurate results in the early transitional flow regime.[19] Based on this experience, we include here the results for the $h = 0.6$ μm case. However, we caution the readers that flow for this case is highly compressible, and it is not fully developed either. Therefore, results for the 0.6-μm-filter diameter case might be invalid because of the aforementioned model limitations.

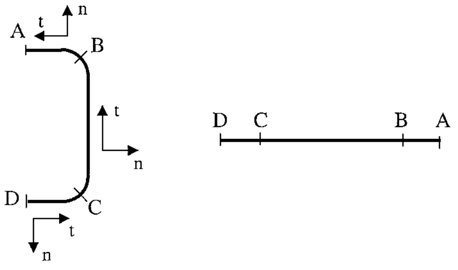

Fig. 3 Curvilinear coordinate system used in Fig. 4.

Rarefaction leads to skin-friction reduction. To demonstrate this, we defined a new coordinate system shown in Fig. 3, which is based on the arc length on the filter surface. In Fig. 4 we present the shear-stress distribution on the left filter surface as a function of the arc length. The values of $x = 0$, 0.19, 0.57, and 0.76 correspond to D, C, B, and A points shown in Fig. 3, respectively. Because we are simulating an array of microfilters, shear stresses on the right surface are mirror images of the ones presented here. Figure 4 shows shear stress acting on the wall at fixed Reynolds number ($Re \approx 7.0$) and at different characteristic dimensions. Because the Reynolds number is fixed while the characteristic dimensions are reduced, the Knudsen number is sequentially increased from cases a to d. Keeping the

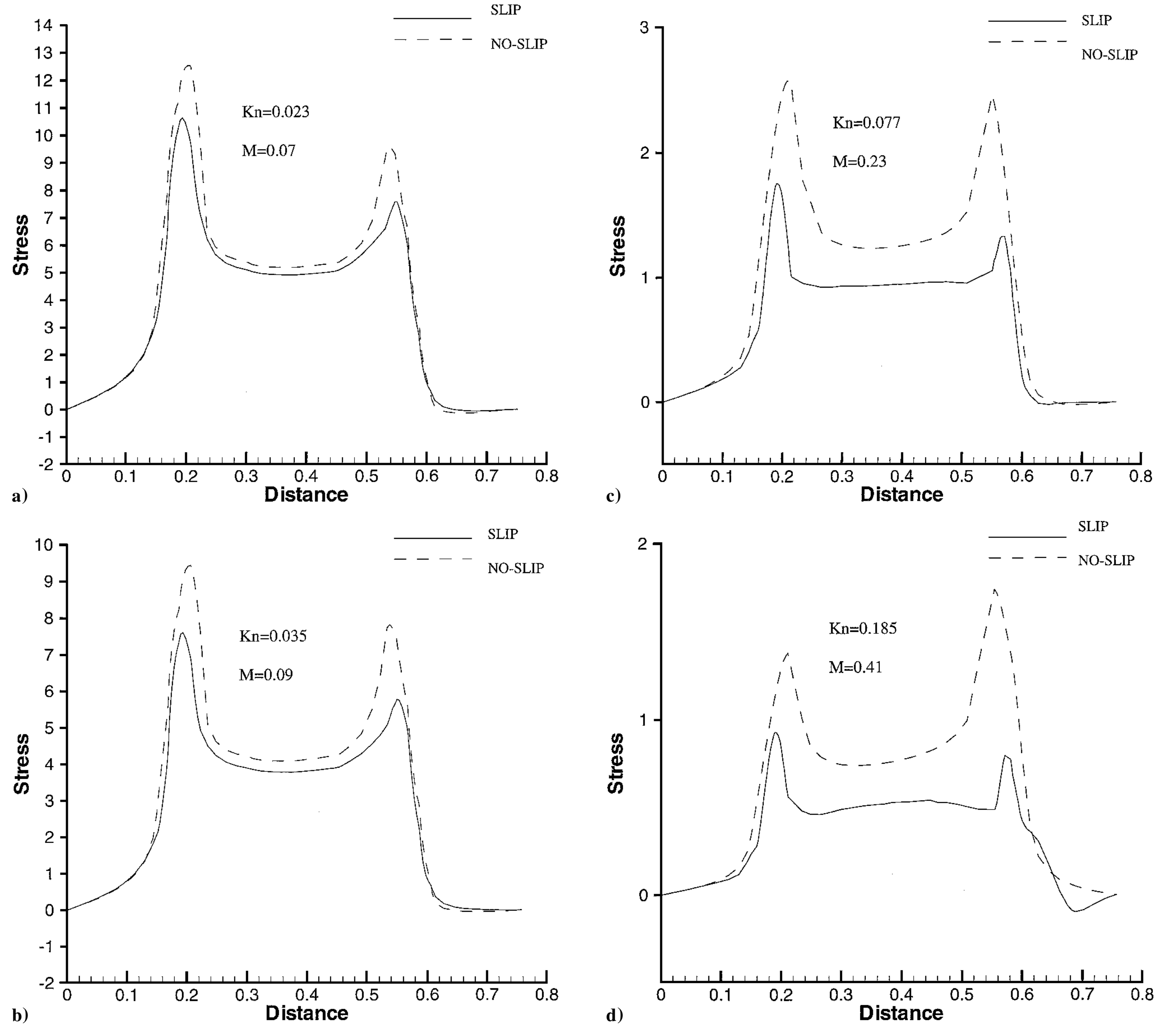

Fig. 4 Shear-stress variation on the surface for a) $L = 6$ μm, b) $L = 4$ μm, c) $L = 2$ μm, and d) $L = 1$ μm cases. The Reynolds number is fixed at $Re \approx 7$ for all four cases. Curvilinear coordinate system used is presented in Fig. 3. The stress values are normalized with the corresponding dynamic head at the domain entrance.

Reynolds number fixed by reducing the characteristic length scale increases the inlet velocity and Mach number. Comparisons of the slip with no-slip cases reveal that shear stresses decrease as a result of the velocity slip on the walls. In Fig. 4d sign reversal in the shear stress indicates local flow separation for this case.

Figure 5 shows the pressure difference between the inlet and outlet control surfaces as a function of the Reynolds number. The filled symbols represent data from the slip flow results, and the no-slip data are presented by the open symbols. This figure verifies that the pressure difference between the front and aft of the body in slip flows is smaller than the corresponding no-slip cases. Here we must note that the total normal stress on a body consists of the pressure and viscous normal stresses. The viscous normal stress on a straight surface is zero for no-slip flows, while finite viscous normal stresses can be obtained for slip flows. Beskok and Karniadakis[20] have shown that the form drag is reduced with increased rarefaction effects, while the viscous normal stresses are increased. Our results also confirm this behavior. However, the magnitudes of the viscous normal stresses are significantly smaller than the pressure differences, and they are not shown here.

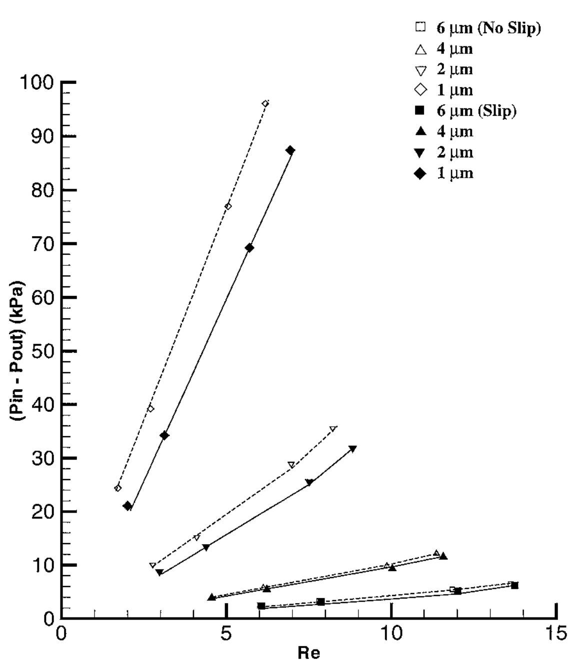

Fig. 5 Pressure difference between the inlet and the exit of microfilters as a function of the Reynolds number.

The streamwise velocity distribution across the middle of the filter is shown in Fig. 6 both for the slip and no-slip cases. The data are taken for fixed Reynolds number case ($Re \approx 7.0$), which corresponds to increased Kn and M, as a result of the decrease in characteristic length scales. Finite slip velocity is observed for all four cases. Comparison of the slip with the corresponding no-slip results shows that the value of the maximum velocity is higher in slip flows. For example in the $Kn = 0.185$ case, the maximum velocity for the slip case is $\approx$225 m/s, whereas for the no-slip case the maximum velocity is $\approx$215 m/s. The velocity profiles are almost parabolic, corresponding to a fully developed channel flow. This is an interesting outcome for a very small channel height to thickness ratio ($h/t = 0.667$), where one expects to observe developing flow profiles. To investigate the reasons of this behavior, we present in Fig. 7 the streamwise velocity distribution obtained before the filter inlet. The flow starts to develop before it reaches the filter inlet at $y/L = 4.3$. For example, at $y/L = 3.0$ the flow is uniform. However at $y/L = 4.0$ the flow starts to slowdown in the filter blockage region ($0.24 < x/L$ and $x/L > 0.76$), and it accelerates in the filter opening area. The velocity distribution becomes almost parabolic at $y/L = 4.24$. This behavior can be explained by the low-Reynolds-number subsonic flow, where the flow starts responding to the upcoming blockage.

To identify the relative magnitude of slip effects and the exact shape of the velocity distribution, we plotted in Fig. 8 the streamwise velocity profiles normalized with the corresponding average velocity:

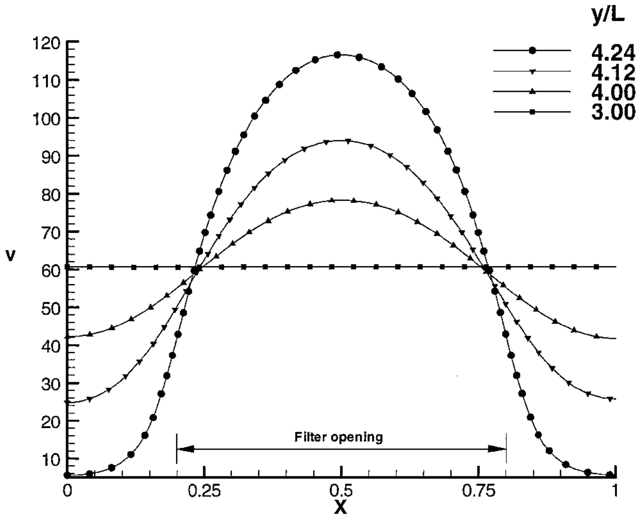

Fig. 7 Velocity profiles upstream of the filter at various y/L locations. The extent of the filter opening is also shown.

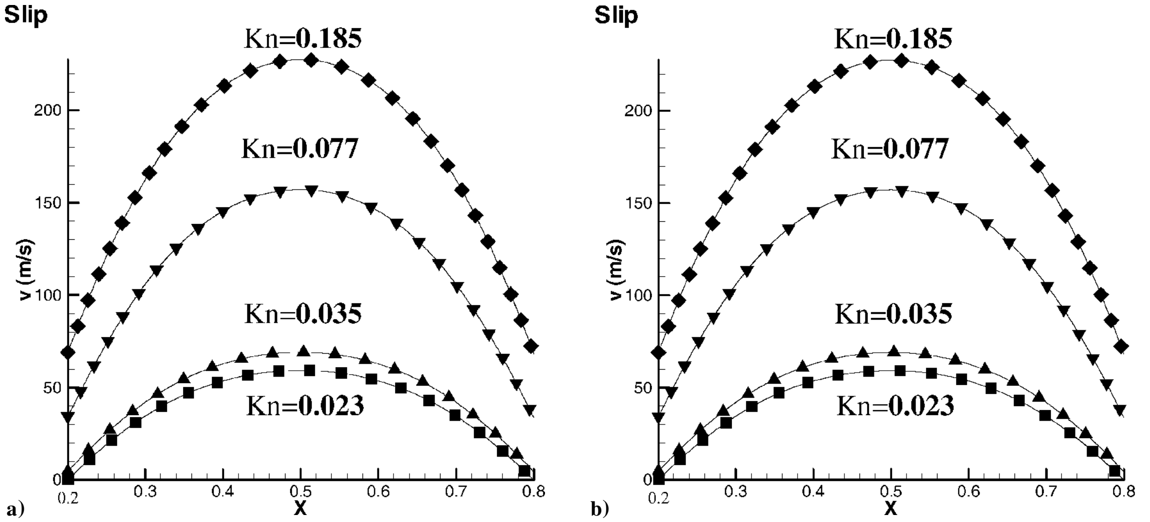

Fig. 6 Streamwise velocity distribution across the filter section for a) slip and b) no-slip flows. The no-slip data are identified with the Knudsen number in the legend in order to correlate the slip and the no-slip results. The simulations correspond to fixed Reynolds number at $Re \approx 7$ and $X = x/L$.

Table 2 Reynolds, Mach, and Knudsen numbers for the current study

	No slip		Slip		
L_{ref}, μm	Re	Ma	Re	Ma	Kn
6	13.61	0.13	13.74	0.13	0.023
6	11.85	0.11	12.02	0.11	0.023
6	7.81	0.07	7.87	0.07	0.023
6	6.01	0.05	6.06	0.05	0.023
4	11.37	0.17	11.58	0.17	0.035
4	9.86	0.14	10.03	0.14	0.035
4	6.12	0.09	6.22	0.09	0.035
4	4.55	0.06	4.55	0.06	0.035
2	8.21	0.27	8.82	0.28	0.078
2	6.96	0.22	7.51	0.23	0.077
2	4.10	0.12	4.39	0.13	0.072
2	2.76	0.08	2.97	0.08	0.072
1	6.20	0.48	6.95	0.51	0.185
1	5.06	0.38	5.71	0.41	0.185
1	2.70	0.18	3.12	0.20	0.162
1	1.71	0.11	1.99	0.12	0.150

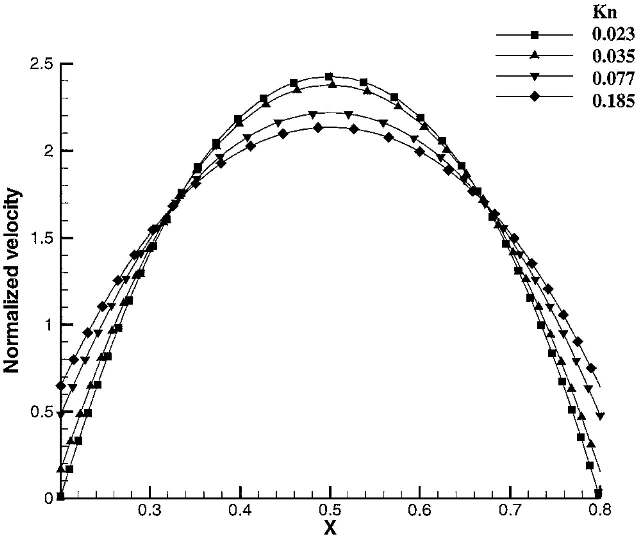

Fig. 8 Streamwise velocity variation of Fig. 6a normalized with the corresponding average velocity. The normalization shows Knudsen-number dependence of the velocity profiles.

$$u^* = \frac{u}{\bar{u}} \qquad \text{where} \qquad \bar{u} = \frac{\int_0^h u(y)\,\mathrm{d}y}{h}$$

It can be seen that the slip velocity increases with the Knudsen number, giving flatter velocity profiles. This has been shown for fully developed isothermal channel flows in Ref. 19, where a unified slip model that is valid in the entire Knudsen regime was proposed in the following form:

$$u^*(y, Kn) = \left[\frac{-(y/h)^2 + y/h + Kn/(1+Kn)}{\frac{1}{6} + Kn/(1+Kn)}\right] \tag{8}$$

Although the velocity profiles seem to be parabolic here, there are slight deviations from a pure parabola, when compared against the unified slip model given by Eq. (8). These differences can be attributed to the developing flow conditions and strong compressibility effects.

Compressibility and Viscous Effects

To investigate the compressibility effects, we fixed the microfilter geometry at $L = 2$ μm and simulated the flow for various inlet speeds. Table 2 shows parameters of this study. The velocity distribution at the middle of the filter for four different inlet conditions are shown in Fig. 9. The maximum velocity in the middle of the filter increases substantially with increased inlet Mach number. The corresponding temperature distribution is also given in Fig. 9. Temperature drops drastically in the middle of the channel for high-Mach-number cases. This drop can be attributed to conversion of thermal energy into kinetic energy, which can also be observed from the velocity results. The temperature jump effects are visible in the temperature profiles, where the gas temperature is seen to be consistently lower than the surface temperature (300 K), indicating net heat transfer into the fluid at this location. Density variations at filter midsection are shown in the bottom figure. Large density variations are observed for high-Mach-number cases, which is a direct indication of the compressibility effect. The compressibility effects are important in all cases, with an exception of the $M = 0.08$ simulation. For low-speed fully developed flows density does not vary substantially across the channels.[16]

Figure 10 shows velocity, temperature, density, and pressure variations along the streamwise direction for the $L = 2$ μm case. In this figure the reference length is fixed, and the inlet velocity is varied, resulting in Reynolds- and Mach-number variations. Streamwise velocity, shown on the top left figure, indicates substantial increases as the flow approaches the filter that is located at $4.3 \leq y/L \leq 4.7$. However, it is clear from the figure that presence of the filter is felt by the flow around $y/L = 3.5$, where the streamwise velocity starts to increase. This observation is consistent with the results shown in Fig. 7. The streamwise velocity starts to decrease after the exit of the channel (at $y/L = 4.7$) and reaches a constant value around $y/L = 6.5$. The figures show only a zoomed up view of the computational domain, where the actual inflow and outflow are located at $y/L = 0$ and 17, respectively. The regions corresponding to large streamwise velocities also experience temperature decrease as shown in Fig. 10. For the high-speed case the temperature drop in the middle of the channel is about 24 K. The minima in temperature is shifting toward the exit of the filter for increased Reynolds- and Mach-number cases. The bottom-left figure shows the density variations in the streamwise direction. Density variation in the domain is a direct indicator of the compressibility effects. The $M = 0.08$ case experiences 10% density drop along the microfilter, and the maximum density variation for the $M = 0.28$ case is about 29%. Pressure variations in the streamwise direction are also shown in Fig. 10, where the differences between the inlet and outlet pressures Δp and inlet to exit pressure ratios can be calculated. The pressure drop starts around $y/L = 3.5$ and becomes severe in the filter section. The pressure, density, and temperature profiles reach constant values almost immediately after the filter section (at $y/L \approx 5.5$). However, the velocity reaches a constant asymptotic value at $y/L \approx 6.5$, depending on the Reynolds number of the flow. In fact, $Re = 8.82$ case requires slightly longer recovery zone than the $Re = 2.97$ case. This is an expected result because of the enhanced inertia of higher-Reynolds-number flows. However the differences are not very significant here because of the relatively small variation in the Reynolds number.

The empirical scaling laws developed for microfilters were discussed earlier in the introduction section. In Fig. 11 we compare our simulation results using the models from Yang et al.[3] and Mott et al.[4] To do this comparison, we used our calculated pressure drop ΔP and normalized it with the dynamic head at the inlet of the channels. Then we used $\beta = 0.6$ and $t/h = 0.667$ to find the values of K'. We plotted K' against the Reynolds number. To be consistent with their definition, we applied the scaling law proposed by Mott et al.,[4] using the inlet Knudsen number (based on the filter hole diameter) in our simulations. We observed some scatter in our results using Mott's model. However, Yang's model resulted in uniformly distributed data with a constant offset. Our data have consistently shown smaller pressure drops than the values reported by Yang et al.[3] The reasons for this can be explained by our modified (smooth) filter geometry shown in Fig. 1. Our filter model had finite radius of curvature at the inlet and exit sections of the filter, and to some degree the filter acts like a micronozzle. The smooth entrance and exit shape with finite radius of curvature $(r/h = 0.1)$ reduces the pressure drop at these locations, resulting in a reduced pressure drop than the experiments and numerical calculations of

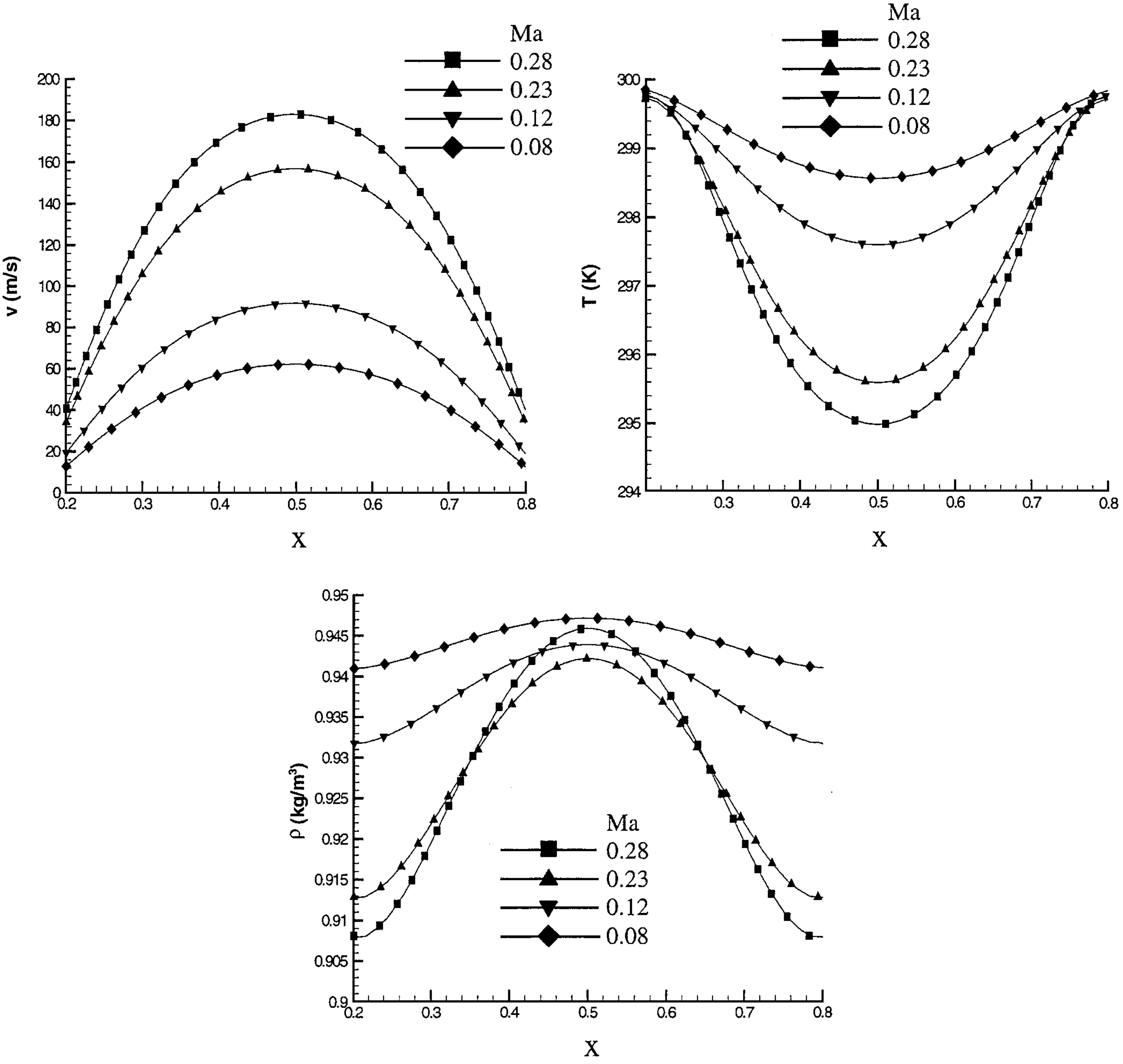

Fig. 9 Streamwise velocity (top left), temperature (top right), and density (bottom) distributions across the filter section for various outlet Mach numbers ($X = x/L$). The wall temperature is fixed at 300 K, which is slightly higher than the local gas temperature as a result of the temperature jump effects. In the bottom figure, rather than the magnitudes of the density, its crossflow variations indicate the compressibility effects.

Yang et al.[3] Strong dependence of the data on the side-wall shape has been demonstrated in Ref. 3 by comparisons of numerical simulations against the experimental data. Besides the differences in the side-wall shapes, three-dimensional flow effects can also be a possible explanation for the disparities between Yang's model and our results. Because the coefficients in these empirical models are dependent on the filter aspect ratio, our inability to match Mott's scaling law can be caused by the extremely small opening factor $\beta = 0.25$ and large t/h ratio used in their studies. Our simulation parameters are closer to Yang's experiments than the values used by Mott et al.[4]

Using the data from our current simulations, we plotted a modified relation for the scaling law as shown in Fig. 12. Because we fixed the t/h ratio in the current study and utilized a finite radius of curvature at the filter inlet and exit ($r/h = 0.1$), we preferred to rewrite the scaling law as

$$K = \beta^{-2}(2.833)\ [10.0/Re + 0.22]$$

where the constant 2.833 is in general a function of t/h and r/h. However, we did not vary these parameters to explore this functional relationship. One also expects an explicit Knudsen-number dependence in the model. This requires further studies beyond the slip flow regime ($Kn > 0.1$), which can be achieved using the DSMC method, such as demonstrated in Ref. 4.

Drag-Force Characteristics

The drag force has two components: viscous drag and form drag. The viscous drag is caused by the accumulative effect of skin-friction distribution on the body in the streamwise direction. The form drag is caused by the differences between the fore and aft pressure distributions on the body in the streamwise direction. Because of the symmetry of the filter geometry and steady flow, we observe zero lift forces at all times. In the top and bottom plots of Fig. 13, we plot the slip and no-slip form-drag and viscous-drag data as a function of the Reynolds number, respectively. A comparison between the no-slip and slip data for the $L = 1$ μm vs $L = 6$ μm cases shows enhanced

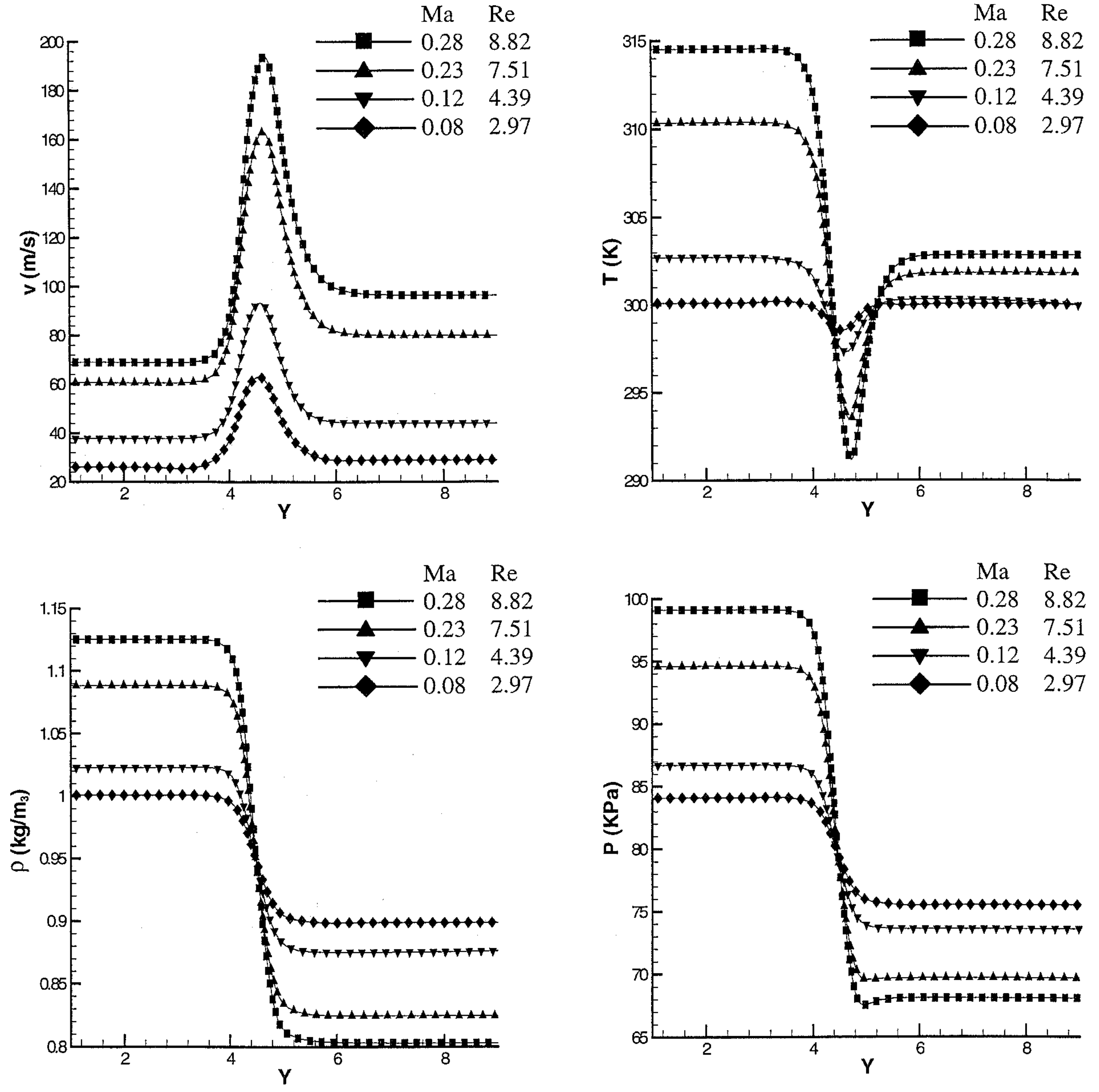

Fig. 10 Variation of streamwise velocity (top left), temperature (top right), density (bottom left), and pressure (bottom right) in the streamwise direction for 2-μm geometry at various Reynolds and Mach numbers ($Y = y/L$).

drag reduction in the smaller geometry, where the Knudsen number is higher. Hence, drag reduction increases by rarefaction. This is an important result, which indicates that the microfilters have the potential to allow more mass flow rate than their macroscale counterparts under fixed inlet and exit pressure conditions, and hence they require less power to operate.

Further examination of Fig. 13 shows that for a fixed geometry both the viscous and form drag increases with the Reynolds number. The increase is mostly linear for low Reynolds numbers and starts to increase faster than linearly for $Re > 10$. We also observed that the viscous drag is consistently about 50% of the form drag. This is important in design of microfilter devices because large drag forces can lead to bursting of thin filter membranes.

Viscous Heating Characteristics

Work done by the viscous stresses usually becomes important for high-speed flows. For example, in the case of the micronozzles viscous heating effects cannot be neglected. In fact, work done by the viscous stresses causes heat generation, which acts as a volumetric source term in the energy equation. In our studies we used a surface integral representation for viscous heating in the following form:

$$\int_{CS} (n_j \tau_{ji}) \cdot u_i \, \mathrm{d}s \tag{9}$$

where τ_{ji} represents ijth component of the viscous stress tensor, n_j shows the jth component of the outward surface normal, u_i shows the ith component of the velocity on the control surface with differential area of ds. To calculate the viscous heating effects, we used the surface of our entire control volume. We also monitored contributions from various portions of the computational domain. For example, the flow is uniform and stress free at most of the periodic surfaces at inflow and outflow regions (The outflow is sufficiently away from the filter here so that velocity field is uniform there). Most of the contributions to the viscous heating effects came from the control surface adjacent to the filter (because of the finite slip velocity and large shear stresses in that region) and the neighboring periodic boundaries.

Figure 14 shows the viscous heating as a function of the Reynolds number for various filter sizes. Smaller filters have shown drastic viscous heating effects. For example, for the 1-μ filter with $Re = 6.95$ ($Ma = 0.51$) the viscous heating per unit filter width can be as large as 1.2 W/m. To keep the Reynolds number within a

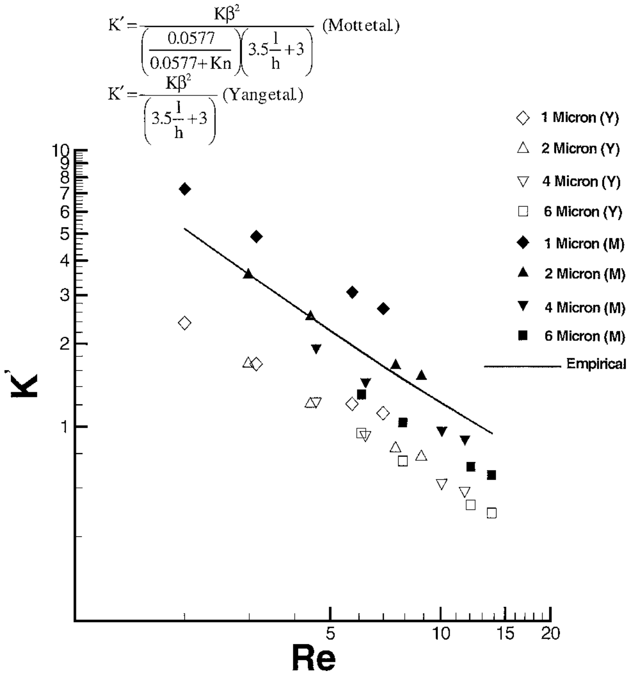

Fig. 11 Comparisons of our simulations against the empirical scaling law developed by Mott et al.[4] (indicated by M) and Yang et al.[3] (indicated by Y).

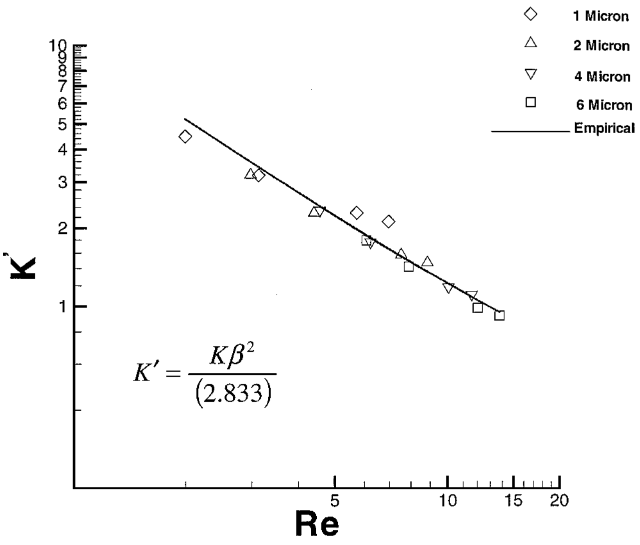

Fig. 12 Modified scaling law that fits the data from our current computations.

certain range, we had to increase the inlet flow speeds substantially, which in return increased the Mach number for small filter dimensions. A comparison of the viscous heating effects shown in Fig. 14 with the reference exit Mach numbers tabulated in Table 2 reveals that the viscous heating effects are important for high-speed flows. Furthermore, increase in the viscous heating as a function of the Reynolds number (or Mach number, as a result of the increase in the reference speed) seems to be faster than linear.

Our numerical algorithm calculates the viscous heating both for the slip and no-slip flows using a volume integral based on the Galerkin formulation. However, rather than using the value of this volume integral we obtained the viscous heating effects by Eq. (9) in the postprocessing stage. Because the velocity on the solid surfaces is zero in no-slip simulations, the boundary integral treatment given by Eq. (9) cannot be utilized for no-slip flows. Nevertheless, we expect viscous heating effects to be higher for the no-slip cases than the slip flows as a result of the reduction in shear stresses and skin friction caused by the slip effects.[20]

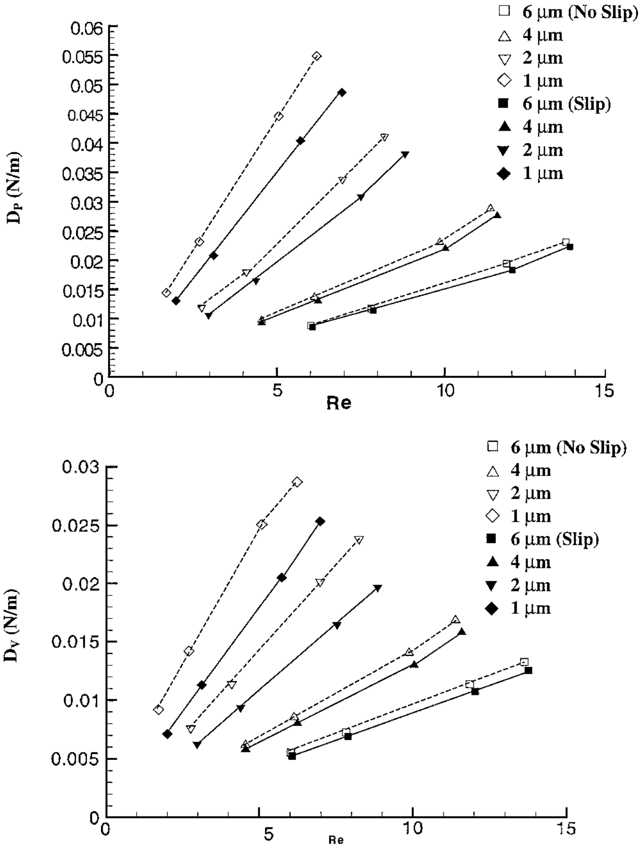

Fig. 13 Top: Form-drag caused by the pressure difference on the front and aft of the surfaces as a function of the Reynolds number. Bottom: Viscous-drag caused by skin friction as a function of the Reynolds number. The results show drag reduction caused by rarefaction, and the viscous drag can be as high as 50% of the form drag.

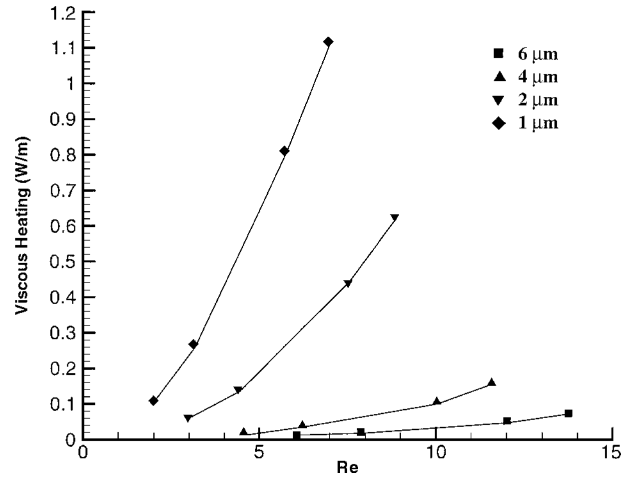

Fig. 14 Viscous heating per unit filter width caused by the work done by viscous stresses.

Conclusions

We performed extensive parametric studies of gas flows through microfilters under various conditions by solving the compressible Navier–Stokes equations with high-order slip and no-slip boundary conditions. The simulation results cover the continuum, slip, and early transitional flow regimes ($Kn < 0.2$). Based on these studies we conclude the following:

1) The rarefaction effects are characterized by the velocity slip and temperature jump conditions in the slip flow regime ($Kn < 0.1$). We have seen that the rarefaction effects result in an overall drag reduction, which affects both the form-drag and the viscous-drag components. We also observed that the viscous drag is as high as 50% of the form drag. Drag reduction can also be interpreted as an increase in the mass flow rate under the same power consumption conditions, which can create certain advantages for microfilter applications.

2) Compressibility effects become important for high-speed flows, which require large pressure drops through the microfilters, leading to large variations in the density as well as the temperature of the fluid. For high-speed flows we observed strong interactions between the temperature and velocity fields, where some thermal energy were locally converted into the kinetic energy.

3) We observed that viscous heating causes significant heat generation in high-speed flows, and it locally impacts the heat-transfer characteristics of microfilters.

4) Our results to some extent matched the empirical scaling law proposed by Yang et al.[3] We believe that the smooth inlet and exit of our filter geometry have resulted in relatively smaller pressure drops than the experiments of Yang et al.,[3] who also considered the side-wall effects on pressure drop through microfilters.

We did not restrict the pressure drops across thin membranes by material strength of the current microfilters. Therefore, some of the pressure drops might be too large for silicon micromachined filters, resulting in bursting of the microfilter elements. Such conditions must be avoided for practical applications.

As a final note, flow through the $L = 1\mu$m case corresponds to the early transitional flow regime, where $Kn > 0.1$. The simulation conditions for this case is beyond the accepted limits of slip flow theory. Therefore, the simulation results for this case may need further validation using a DSMC algorithm.

Acknowledgment

This work has been supported by the Oak Ridge Associated Laboratories, Ralph E. Powe Junior Faculty Enhancement Award, 2000.

References

[1] Chu, W.-H., Chin, R. C., and Huen, T., "Silicon Membrane Nanofilters from Sacrificial Oxide Removal," *Journal of Microelectromechanical Systems*, Vol. 8, No. 1, 1999, pp. 34–42.

[2] Yang, X., Yang, J. M., Tai, Y. C., and Ho, C. M., "Micromachined Membrane Particle Filters," *Sensors and Actuators A: Physical*, Vol. 73, No. 1–2, 1999, pp. 184–191.

[3] Yang, J. M., Yang, X., Ho, C. M., and Tai, Y.-C., "Micromachined Particle Filter with Low Power Dissipation," *Journal of Fluids Engineering*, Vol. 123, 2001, pp. 899–980.

[4] Mott, D. R., Oran, E. S., and Kaplan, C. R., "Microfilter Simulations and Scaling Laws," *Journal of Thermophysics and Heat Transfer*, Vol. 15, No. 4, 2001, pp. 473–477.

[5] Harley, J. C., Huang, Y., Bau, H. H., and Zemel, J. N., "Gas Flow in Micro Channels," *Journal of Fluid Mechanics*, Vol. 284, 1995, pp. 257–274.

[6] Liu, J. Q., Tai, Y. C., Pong, K. C., and Ho, C. M., "Micromachined Channel/Pressure Sensor Systems for Micro Flow Studies," *7th International Conference on Solid-State Sensors and Actuators*, Inst. of Electrical Engineers of Japan, Yokohama, Japan, 1993, pp. 995–998.

[7] Pong, K. C., Ho, C. M., Liu, J., and Tai, Y. C., "Non-Linear Pressure Distribution in Uniform Microchannels," *Application of Microfabrication to Fluid Mechanics*, Vol. 197, American Society of Mechanical Engineers, New York, 1994, pp. 51–56.

[8] Arkilic, E. B., Schmidt, M. A., and Breuer, K. S., "Gaseous Slip Flow in Long Microchannels," *Journal of Microelectromechanical Systems*, Vol. 6, No. 2, 1997, pp. 167–178.

[9] Arkilic, E. B., Breuer, K. S., and Schmidt, M. A., "Gaseous Flow in Microchannels," *Application of Microfabrication to Fluid Mechanics*, Vol. 197, American Society of Mechanical Engineers, New York, 1994, pp. 57–66.

[10] Shih, J. C., Ho, C. M., Liu, J., and Tai, Y. C., "Monotomic and Polyatomic Gas Flow Through Uniform Microchannels," *Microelectromechanical Systems*, Vol. 59, American Society of Mechanical Engineers, New York, 1996, pp. 197–207.

[11] Weighardt, K. E. G., "On the Resistance of Screens," *Aeronautical Quarterly*, Vol. 4, 1953, pp. 186–192.

[12] Derbunovich, G. I., Zamskaya, A. S., Repik, Y. U., and Sosedko, Y. P., "Hydraulic Drag on Perforated Plates," *Fluid Mechanics-Soviet Research*, Vol. 13, 1998, pp. 111–116.

[13] Kittilsland, G., Steme, G., and Nordoen, B. A., "Submicron Particle Filter in Silicon," *Sensors and Actuators A: Physical*, Vol. 23, 1990, pp. 904–907.

[14] Maxwell, J. C., "On Stresses in Rarified Gases Arising from Inequalities of Temperature," *Philosophical Transactions of the Royal Society Part I*, Vol. 170, 1879, pp. 231–256.

[15] von Smoluchowski, M., "Ueber Wärmeleitung in Verdünnten Gasen," *Annalen der Physik und Chemie*, Vol. 64, 1898, pp. 101–130.

[16] Beskok, A., Trimmer, W., and Karniadakis, G. E., "Rarefaction and Compressibility Effects in Gas Microflows," *Journal of Fluids Engineering*, Vol. 118, No. 3, 1996, pp. 448–456.

[17] Beskok, A., and Karniadakis, G. E., *Microflows: Fundamentals and Simulation*, Springer, New York, 2001, pp. 53–62, 224–239.

[18] Ahmed, I., "Simulation of Gas Flows Through Micro-Constrictions," M.S. Thesis, Mechanical Engineering Dept., Texas A&M Univ., College Station, TX, May 2001.

[19] Beskok, A., and Karniadakis, G. E., "A Model for Flows in Channels, Pipes and Ducts at Micro and Nano Scales," *Microscale Thermophysical Engineering*, Vol. 3, No. 1, 1999, pp. 43–77.

[20] Beskok, A., and Karniadakis, G. E., "Simulation of Heat and Momentum Transfer in Complex Microgeometries," *Journal of Thermophysics and Heat Transfer*, Vol. 8, No. 4, 1994, pp. 647–655.